Numerical simulation of liquid sloshing in a partially filled container with inclusion of compressibility effects

Y. G. Chen[a] and W. G. Price[b]
School of Engineering Sciences, Ship Science, University of Southampton, Southampton SO17 1BJ, United Kingdom

(Received 8 July 2009; accepted 14 October 2009; published online 19 November 2009)

A numerical scheme of study is developed to model compressible two-fluid flows simulating liquid sloshing in a partially filled tank. For a two-fluid system separated by an interface as in the case of sloshing, not only a Mach-uniform scheme is required but also an effective way to eliminate unphysical numerical oscillations near the interface. By introducing a preconditioner, the governing equations expressed in terms of primitive variables are solved for both fluids (i.e., water, air, gas, etc.) in a unified manner. In order to keep the interface sharp and to eliminate unphysical numerical oscillations in unsteady fluid flows, the nonconservative implicit split coefficient matrix method is modified to construct a flux-difference splitting scheme in the dual-time formulation. The proposed numerical model is evaluated by comparisons between numerical results and measured data for sloshing in an 80% filled rectangular tank excited at resonance frequency. Through similar comparisons, the investigation is further extended by examining sloshing flows excited by forced sway motions in two different rectangular tanks with 20% and 83% filling ratios. These examples demonstrate that the proposed method is suitable to capture induced free surface waves and to evaluate sloshing pressure loads acting on the tank walls and ceiling. © *2009 American Institute of Physics*. [doi:10.1063/1.3264835]

I. INTRODUCTION

The effect of dispersed bubbles or entrapped air in a two-fluid sloshing flow is important when the excited surface wave impacts on the sides or roof of a container.[1] When a wave breaks or is near to breaking as it hits a wall, air often becomes trapped. The presence of air as a trapped bubble or dispersed air, or most likely a combination of both, has a cushioning effect and local pressures are then influenced by the compressibility of the air.[2–4] Therefore, investigations of compressibility effects of gas and liquid in violent sloshing motions provide improved insights and understanding of the complicated hydrodynamic phenomena occurring in high-speed impacts on tank walls, air bubble entrapment, breaking waves, and so on.

To compute compressible multifluid flows arising in liquid sloshing in a partially filled moving tank, there are two major issues that need resolving. The first requires the development of a unified method to solve conditions varying from weakly compressible flows to high-speed flows. The standard methods adopted to solve compressible flows based on the hyperbolic conservation laws are neither numerically robust nor efficient in the case of low Mach number or weak compressibility (the incompressible limit).[5–7] For many algorithms preconditioning techniques are a necessity in order to obtain a converged solution at low speeds.[7–11] Another issue is that for any standard conservative, shock-capturing scheme to compute multifluid systems, pressure oscillations exist intrinsically near the interface surface.[12,13] In a compressible two-fluid flow computation, pressures (densities) are used for further computations, such as the computation of densities (pressure) from their equations of state, which give rise to numerically based oscillations near the interface and finally cause deterioration of the whole flow field at subsequent times. Such oscillations are present in first-order computations and do not decrease with decreasing the mesh size in any interface capturing method other than a tracking method.[14] The interfacial correction method based on an exact Riemann solver proposed by Cocchi *et al.*,[15] Davis,[16] and Igra,[17] locally nonconservative fixes suggested by Abgrall[18] and the ghost fluid method introduced by Fedkiw *et al.*[19] are the best known approaches to overcome the described difficulties.

In this study, a preconditioner is introduced to solve multifluid flows in a unified manner. The present approach combines the preconditioning technique with an implicit split coefficient matrix method (SCMM) scheme to ensure the generation of a numerical method applicable to both incompressible and compressible flow regimes and devoid of numerically induced pressure oscillations near the interface. This requires the application of a dual-time preconditioning technique[11] to the two-fluid flows. A characteristic-based primitive-variable flux-difference splitting method related to the SCMM scheme[20] is employed to reduce interface diffusion and eliminate numerical spurious oscillations with the level set approach adopted to capture the free surface characteristic.[21]

[a]Author to whom correspondence should be addressed. Telephone: +44 8059 6524. Fax: +44 8059 3299. Electronic mail: y.chen@soton.ac.uk.
[b]Electronic mail: w.g.price@soton.ac.uk.

II. THEORETICAL FORMULATION

A. Three-dimensional governing equations

The fluid motion in liquid and gas phases are both assumed to be compressible. This two-fluid system is assumed immiscible and adiabatic, and fluid density ρ is only a function of pressure p, e.g., $\rho=\rho(p)$. The basic equations describing the two-fluid system are expressed in Cartesian coordinates as

$$\frac{\partial \rho}{\partial t}+\frac{\partial(\rho u_j)}{\partial x_j}=0, \tag{1}$$

$$\frac{\partial(\rho u_i)}{\partial t}+\frac{\partial(\delta_{ij}p)}{\partial x_j}+\frac{\partial(\rho u_i u_j)}{\partial x_j}-\frac{\partial}{\partial x_j}\left(\frac{2\mu}{\mathrm{Re}}s_{ij}\right)=-\frac{\rho g_i}{\mathrm{Fn}^2}-\rho f_i. \tag{2}$$

A conventional Cartesian tensor notation is adopted in these two equations. The spatial coordinates x_i $(i=1,2,3)$, velocity components u_i, and projection components of the gravitational acceleration in the axis directions g_i, respectively, have been nondimensionalized for each specific problem in terms of a characteristic length L, a characteristic velocity U_0, and gravitational acceleration g. The fluid density ρ and viscosity μ are nondimensionalized by their respective water reference values ρ_w and μ_w at a prescribed state; the time t and the pressure p variables are nondimensionalized by L/U_0 and $\rho_w U_0^2$, respectively. The Reynolds number, Re, Froude number, Fn, and strain rate tensor s_{ij} are defined by

$$\mathrm{Re}=LU_0/\nu_w, \quad \mathrm{Fn}=U_0/\sqrt{Lg}, \qquad s_{ij}=\frac{1}{2}\left(\frac{\partial u_i}{\partial x_j}+\frac{\partial u_j}{\partial x_i}\right). \tag{3}$$

With the exception of the gravitational force, the external forces include the translational and rotational inertia forces, and f_i takes the following form:

$$f_i=a_i+\varepsilon_{ijk}\frac{d\omega_j}{dt}x_k+\varepsilon_{ijk}\varepsilon_{klm}\omega_j\omega_l x_m+2\varepsilon_{ijk}\omega_j u_k, \tag{4}$$

where a_i represents the translational acceleration components and ω_i represents the rotational angular velocity components. Here ε_{ijk} denotes the Levi-Civita symbol with repeating subscripts indicating summation. The effect of surface tension is neglected in this mathematical model.

To simulate fluid sloshing problems encountered in the field of ship hydrodynamics, the gas and liquid are both assumed adiabatic and their thermodynamic behavior is described by an equation of state. For example, the Tait equation of state[14] is employed for water and the ideal gas equation of state for air is used with different parameter values. They have the following unified form:

$$\frac{p+B}{p_0+B}=\left(\frac{\rho}{\rho_0}\right)^{\gamma}, \tag{5}$$

where p_0 and ρ_0 are the reference pressure and density values, respectively. For example, for water, the constants B and γ are given by $B_w=296.3\times10^{+6}$ and $\gamma_w=7.415$, and for air by $B_a=0$ and $\gamma_a=1.4$. In terms of Eq. (5), the speed of sound for each fluid phase is calculated from the following equation:

$$c=\sqrt{\frac{\partial p}{\partial \rho}}=\sqrt{\frac{\gamma(B+p)}{\rho}}.$$

B. Free surface capturing method

The free surface is defined as the zero level set of a level set function ϕ initialized as a signed distance function from the interface. In air, ϕ is set to a positive value and in water to a negative value as defined by

$$\begin{cases}\phi(x_1,x_2,x_3;t)>0 & \text{in} \quad \text{air},\\ \phi(x_1,x_2,x_3;t)=0 & \text{on} \quad \text{surface},\\ \phi(x_1,x_2,x_3;t)<0 & \text{in} \quad \text{water}.\end{cases} \tag{6}$$

Differentiating $\phi=0$ with respect to time t, a transport equation is derived to describe the free surface motion in the form

$$\frac{\partial \phi}{\partial t}+u_i\frac{\partial \phi}{\partial x_i}=0, \tag{7}$$

where u_i is the local fluid velocity and, at any time, moving the interface is equivalent to updating ϕ by solving Eq. (7).

Due to the sharp change in properties of fluids at the interface, we introduce a region of finite thickness over which a smooth but rapid change in density and viscosity occurs across the interface.

First, we define a smoothed Heaviside function $H_\varepsilon(x)$ satisfying

$$H_\varepsilon(x)=\begin{cases}1 & \text{if} \quad x>\varepsilon,\\ 0 & \text{if} \quad x<-\varepsilon,\\ 0.5(x+\varepsilon)/\varepsilon+0.5\sin(\pi x/\varepsilon)/\pi & \text{otherwise},\end{cases} \tag{8}$$

where ε is half the finite thickness of the interface in which the density and viscosity change.[22]

Using the above function, we can define the corresponding smoothed viscosity function μ as

$$\mu_\varepsilon(\phi)=[1-H_\varepsilon(\phi)]+\frac{\mu_a}{\mu_w}H_\varepsilon(\phi). \tag{9}$$

The density is updated by means of the equation of state. The two nondimensional densities $\rho_1=[p/(p_0+B_w)+1]^{1/\gamma_w}$ and $\rho_2=\rho_a/\rho_w[(p/p_0)+1]^{1/\gamma_a}$ are evaluated from Eq. (5) using the pressure value at a grid point and the corresponding smoothed density function ρ is defined as

$$\rho_\varepsilon(\phi)=\rho_1[1-H_\varepsilon(\phi)]+\rho_2 H_\varepsilon(\phi), \tag{10}$$

where the constant B_w and reference pressure p_0 are nondimensional quantities. The gauge pressure (i.e., the reference pressure subtracted from the absolute pressure) is used in order to reduce the effect of round-off errors at low speed fluid flows.

Even if we initialize ϕ as a signed distance from a wave front, the level set function no longer remains a distance function at later times. For numerical reasons, the level set function is reinitialized so that ϕ satisfies $|\nabla\phi|=1$. An iterative procedure is used at each time step[22] by solving the following Hamilton–Jacobi equation:

$$\frac{\partial\phi}{\partial t}=\mathrm{sgn}(\phi_0)(1-|\nabla\phi|),$$
$$\phi(x_1,x_2,x_3;t)=\phi_0(x_1,x_2,x_3), \tag{11}$$

where sgn denotes the sign function. Given a level set function, ϕ_0, at time t, the previous equation has the property that the steady state solution ϕ has the same sign and same zero level set as ϕ_0, and converges to $|\nabla\phi|=1$. Therefore, it is a distance function to the wave front. For numerical reasons,[22] this sign function is approximated by

$$S_\varepsilon(\phi_0)=\frac{\phi_0}{\sqrt{\phi_0^2+\varepsilon^2}}.$$

During the reinitialization exercise a numerical procedure developed by Sussman *et al.*[23] was introduced to preserve the fluid volume in each cell to improve the accuracy of solution of Eq. (11). In the numerical experiments described in Sec. IV, this improved level set method[23] was adopted and it produced a significant improvement to the accuracy of capturing free surface waves.

C. Preconditioning dual-time technique

In solving the compressible equations for low Mach number, the acoustic eigenvalues are much higher than the convective ones. For the sake of stability the time step increment must be chosen inversely proportional to the highest eigenvalue of the system to satisfy the Courant–Friedrichs–Lewy condition.[24] This implies that other waves convected at fluid speed do not change very much over a time step and thousands of time steps may be required for them to reach a steady state value. Hence, the standard methods for compressible flows based on the hyperbolic conservation laws are neither numerically robust nor efficient in the case of low Mach number or weak compressibility.

In this study, primitive variables, rather than conservative variables, are employed to evolve time-dependent Reynolds-Averaged Navier–Stokes equations. The preconditioning technique developed for compressible single phase flows by changing the eigenvalues of the system[7,11] is extended to compressible two-fluid flow problems associated with liquid sloshing in partially filled containers. An important feature of the proposed method is that the compressible gas and liquid equations are unified to a single system, e.g., a single phase flow, and in each time step both phases are updated simultaneously. The interface is only treated as a variation in fluid properties.

In terms of generalized coordinates, Eqs. (1) and (2) with the addition of a preconditioned pseudotime derivative can be rewritten in a vector form as given by

$$\Gamma_\tau\frac{\partial q}{\partial\tau}+\frac{\partial Q}{\partial t}+\frac{\partial F_j}{\partial\xi_j}+\frac{\partial F_j^\nu}{\partial\xi_j}=S, \tag{12}$$

where vectors q, Q, F_j, F_j^ν, and S are expressed as

$$q=J^{-1}(p,u,v,w)^T,\quad Q=J^{-1}(\rho_\varepsilon,\rho_\varepsilon u,\rho_\varepsilon v,\rho_\varepsilon w)^T,$$

$$F_j=J^{-1}\begin{bmatrix}\rho U^j\\ \rho_\varepsilon u_1U^j+\frac{\partial\xi^j}{\partial x_1}p\\ \rho_\varepsilon u_2U^j+\frac{\partial\xi^j}{\partial x_2}p\\ \rho_\varepsilon u_3U^j+\frac{\partial\xi^j}{\partial x_3}p\end{bmatrix},$$

$$F_j^\nu=J^{-1}\frac{\mu_\varepsilon}{\mathrm{Re}}\frac{\partial\xi_j}{\partial x_m}\left(0,\frac{\partial\xi_k}{\partial x_m}\frac{\partial u}{\partial\xi_k}+\frac{\partial\xi_k}{\partial x}\frac{\partial u_m}{\partial\xi_k},\frac{\partial\xi_k}{\partial x_m}\frac{\partial v}{\partial\xi_k}+\frac{\partial\xi_k}{\partial y}\frac{\partial u_m}{\partial\xi_k},\frac{\partial\xi_k}{\partial x_m}\frac{\partial w}{\partial\xi_k}+\frac{\partial\xi_k}{\partial z}\frac{\partial u_m}{\partial\xi_k}\right)^T,$$

$$S=J^{-1}\rho_\varepsilon(0,f_1+g_1/\mathrm{Fn}^2,f_2+g_2/\mathrm{Fn}^2,f_3+g_3/\mathrm{Fn}^2)^T.$$

Here $J=\partial(\xi,\eta,\zeta)/\partial(x,y,z)$ is the Jacobian of the transformation and the contravariant velocity component U^j is defined as

$$U^j=\frac{\partial\xi_j}{\partial x_m}u_m.$$

To optimize the performance of the pseudoiteration, the pseudotime term is written in terms of the primitive variables. The preconditioning step consists of the replacement of matrix Γ_τ by a matrix defined by

$$\Gamma_\tau=\begin{bmatrix}1/V_r^2 & 0 & 0 & 0\\ u/V_r^2 & \rho_\varepsilon & 0 & 0\\ v/V_r^2 & 0 & \rho_\varepsilon & 0\\ w/V_r^2 & 0 & 0 & \rho_\varepsilon\end{bmatrix}.$$

Here, V_r is the reference velocity which is chosen to ensure that the system is well conditioned at low speed and to accelerate convergence. In practice, this parameter is generally defined as some functional combination of the free stream and the local convective velocities.[7,11]

III. NUMERICAL METHOD

The implementation of the preconditioned dual-time algorithm is now discussed adopting two different discretization strategies. The conservative Roe's flux-difference splitting method[25] is presented to solve the compressible single phase fluid flow, whereas the nonconservative SCMM or a hybrid combining both schemes of presentation is used for the compressible two-fluid flow.

For the sake of simplicity in Sec. III A, only the convective flux derivative in one direction is presented, and the viscous and source terms in Eq. (12) are omitted. For example, we denote by F the convective flux F_1 in the ξ-direction.

A. Preconditioned Roe's flux-difference formulations

First let us consider Roe's approximate Riemann scheme,[25] which is given by

$$\tilde{F}_{j+1/2} = \tfrac{1}{2}[F(Q^L_{j+1/2}) + F(Q^R_{j+1/2}) - |A(Q^L_{j+1/2}, Q^R_{j+1/2})| \times (Q^R_{j+1/2} - Q^L_{j+1/2})]. \tag{13}$$

Roe's method provides an exact solution to an approximate Riemann problem by evaluating the Jacobian matrix A of the convective flux vector F as Roe-averaged variables dependent on left and right states $Q^L_{j+1/2}$ and $Q^R_{j+1/2}$ at the interface $\xi=\xi_{j+1/2}$. In this expression, $|A|=T|\Lambda|T^{-1}$, where T is the matrix whose columns are the right eigenvectors of A, T^{-1} is the matrix whose rows are the left eigenvectors of A, and $|\Lambda|$ is a diagonal matrix whose elements are the absolute values of the eigenvalues of A.

By implicitly discretizing Eq. (12) with a first-order finite difference scheme for the pseudotime and a second-order backward difference approximation for the physical time terms, we have

$$\Gamma_\tau \frac{q^{m+1,n+1} - q^{m,n+1}}{\Delta\tau} + \frac{1.5Q^{m+1,n+1} - 2Q^n + 0.5Q^{n-1}}{\Delta t} + \delta_\xi F^{m+1,n+1} = 0. \tag{14}$$

Here, the superscript n denotes the nth physical time level, the superscript m the level of the subiteration, and δ_ξ represents a spatial difference. After linearizing terms at the $(m+1)$th time level and involving some simple algebraic manipulation, the above equation becomes

$$\left(\Gamma_\tau + M\frac{3\Delta\tau}{2\Delta t} + A_q\Delta\tau\delta_\xi\right)\delta_\tau q + \delta_\xi F^{m,n+1} = r^{m,n+1}, \tag{15}$$

where δ_τ represents the pseudotime difference, and $A_q = \partial F/\partial q$, $M = \partial Q/\partial q$, and

$$r^{m,n+1} = -\frac{1.5Q^{m,n+1} - 2Q^n + 0.5Q^{n-1}}{\Delta t}.$$

Let us define $\Gamma_d = \Gamma_\tau + M(3\Delta\tau/2\Delta t)$ as the nonconservative variable preconditioning matrix. Multiplying both sides of Eq. (15) by the inverse Γ_d^{-1}, we derive the result

$$(I + a_q\Delta\tau\delta_\xi)\delta_\tau q + a_q\delta_\xi q = \Gamma_d^{-1} r, \tag{16}$$

where it is easily verified that the preconditioned flux Jacobian matrix and the Roe numerical flux expression in terms of primitive variables are, respectively, given by

$$a_q = \Gamma_d^{-1} A_q,$$
$$\tilde{F}_{j+1/2} = \tfrac{1}{2}(F^L + F^R) - \tfrac{1}{2}\hat{\Gamma}_d|\hat{a}_q|\Delta q. \tag{17}$$

Here the tilde over each term means that they are evaluated using the Roe-averaged variables.

Furthermore, the transformation of Eq. (16) into conservative variables gives

$$(I + a\Delta\tau\delta_\xi)\delta_\tau Q + a\delta_\xi Q = M\Gamma_d^{-1} r. \tag{18}$$

It now follows that the system matrix for the vector Q is given by

$$a = Ma_qM^{-1} = M\Gamma_d^{-1}A_qM^{-1} = M\Gamma_d^{-1}A$$

and the corresponding numerical flux at a cell interface, analogous to Eq. (17), is defined as

$$\tilde{F}_{j+1/2} = \tfrac{1}{2}(F^L + F^R) - \tfrac{1}{2}\hat{\Gamma}_d\hat{M}^{-1}|\hat{a}|\Delta Q, \tag{19}$$

where the matrix $\Gamma_d M^{-1}$ is defined as the conservative variable preconditioning matrix.

Since Eqs. (16) and (18) with the corresponding Roe's numerical fluxes in Eqs. (17) and (19) are equivalent, the two methods described here are conservative but do not satisfy the discrete Rankine–Hugoniot jump conditions to ensure exact recognition of isolated discontinuities such as a shock wave.

B. Preconditioned SCMM formulation

The basic idea behind the nonconservative SCMM scheme[26] is to split the Jacobian coefficient matrix into two submatrices, each associated with the positive or negative eigenvalues of the Jacobian. Hence, a one-sided finite difference scheme can be applied to each split flux difference.

The multiplication of both sides of Eq. (16) by Γ_d and implementing the similarity transform for the Jacobian matrix $a_q = T\Lambda T^{-1}$ leads to

$$(\Gamma_d + \Delta\tau\Gamma_d T\Lambda T^{-1}\delta_\xi)\delta_\tau q + \Gamma_d T\Lambda T^{-1}\delta_\xi q = r. \tag{20}$$

Here the diagonal matrix Λ consists of the eigenvalues of a_q and T is the matrix of its right eigenvectors.

The implementation of positive and negative decomposition of the Jacobian matrix and by defining the positive and negative nonconservative flux differences as

$$\delta_\xi F^+ = \Gamma_d T\Lambda^+ T^{-1}\delta_\xi q = \Gamma_d a_q^+\delta_\xi q = \bar{a}_q^+\delta_\xi q,$$
$$\delta_\xi F^- = \Gamma_d T\Lambda^- T^{-1}\delta_\xi q = \Gamma_d a_q^-\delta_\xi q = \bar{a}_q^-\delta_\xi q$$

allow Eq. (20) to be expressed in the form

$$(\Gamma_d + \Delta\tau\bar{a}^+\delta_\xi + \Delta\tau\bar{a}^-\delta_\xi)\delta_\tau q = r - \delta_\xi F^+ - \delta_\xi F^-, \tag{21}$$

where the plus (minus) eigenvalue matrices are given by

$$\Lambda^\pm = \tfrac{1}{2}(\Lambda \pm |\Lambda|).$$

The first-order upwind difference approximation to the positive and negative flux differences at a node j is

$$\delta_\xi F^+ + \delta_\xi F^- \approx \bar{a}_q^+(\bar{q}_{j-1/2})(q_j - q_{j-1}) + \bar{a}_q^-(\bar{q}_{j+1/2})(q_{j+1} - q_j), \tag{22}$$

where $\bar{q}_{j+1/2}$ is the arithmetic average of the primitive variables q_j and q_{j+1}.

Higher order spatial discretizations were derived by Lombard *et al.*[26] For example, the second-order upwind and third order upwind-biased methods are defined, respectively, by

$$\frac{3}{2}\bar{a}_q^+(\bar{q}_{j-1/2})\delta_\xi q - \frac{1}{2}\bar{a}_q^+(\bar{q}_{j-3/2})\delta_\xi q + \frac{3}{2}\bar{a}_q^-(\bar{q}_{j+1/2})\delta_\xi q - \frac{1}{2}\bar{a}_q^-(\bar{q}_{j+3/2})\delta_\xi q \tag{23}$$

and

$$\frac{1}{3}\bar{a}_q^+(\bar{q}_{j+1/2})\delta_\xi q + \frac{5}{6}\bar{a}_q^+(\bar{q}_{j-1/2})\delta_\xi q - \frac{1}{6}\bar{a}_q^+(\bar{q}_{j-3/2})\delta_\xi q + \frac{1}{3}\bar{a}_q^-(\bar{q}_{j-1/2})\delta_\xi q + \frac{5}{6}\bar{a}_q^-(\bar{q}_{j+1/2})\delta_\xi q - \frac{1}{6}\bar{a}_q^-(\bar{q}_{j+3/2})\delta_\xi q. \tag{24}$$

The SCMM scheme based on the primitive variables as described, although it eliminates numerical spurious oscillations near the interface, is nonconservative. This implies that this numerical scheme of study can only be applied to low Mach number flows, transonic flow, or to a problem involving the simultaneous presence of both.

C. Eigensystem and numerical convective fluxes

The nonconservative variable preconditioning matrix Γ_d in Eqs. (16) and (20) has the form

$$\Gamma_d = \Gamma_\tau + \frac{3\Delta\tau}{2\Delta t}M = \begin{bmatrix} b_1 & 0 & 0 & 0 \\ ub_1 & b_2 & 0 & 0 \\ vb_1 & 0 & b_2 & 0 \\ wb_1 & 0 & 0 & b_2 \end{bmatrix}, \tag{25}$$

where $b_1 = (1/V_r^2) + (1.5\Delta\tau/\Delta t)(1/c^2)$ and $b_2 = \rho_\varepsilon[1 + (1.5\Delta\tau/\Delta t)]$.

The preconditioned inviscid flux Jacobian matrix a_q in Eqs. (16) and (20) is expressed as

$$a_q = \Gamma_d^{-1}A_q = \begin{bmatrix} U^1/(c^2b_1) & \rho_\varepsilon\frac{\partial\xi}{\partial x}/b_1 & \rho_\varepsilon\frac{\partial\xi}{\partial y}/b_1 & \rho_\varepsilon\frac{\partial\xi}{\partial z}/b_1 \\ \frac{\partial\xi}{\partial x}/b_2 & \rho_\varepsilon U^1/b_2 & 0 & 0 \\ \frac{\partial\xi}{\partial y}/b_2 & 0 & \rho_\varepsilon U^1/b_2 & 0 \\ \frac{\partial\xi}{\partial z}/b_2 & 0 & 0 & \rho_\varepsilon U^1/b_2 \end{bmatrix} \tag{26}$$

and its eigenvalues are given by

$$\lambda_1 = \lambda_2 = \rho_\varepsilon U^1/b_2,$$
$$\lambda_{3,4} = \frac{\rho_\varepsilon U^1}{2}\left(\frac{1}{b_2} + \frac{1}{\rho_\varepsilon c^2 b_1}\right) \pm \sqrt{\left(\frac{\rho_\varepsilon U^1}{2b_2}\right)^2 + \frac{\rho_\varepsilon}{b_1 b_2}\frac{\partial\xi}{\partial x_j}\frac{\partial\xi}{\partial x_j} + \left(\frac{U^1}{2c^2b_1}\right)^2 - \frac{\rho_\varepsilon (U^1)^2}{2c^2 b_1 b_2}} \equiv \frac{\rho_\varepsilon U^1}{2}\left(\frac{1}{b_2} + \frac{1}{\rho_\varepsilon c^2 b_1}\right) \pm \Delta. \tag{27}$$

The eigenvectors associated with the four eigenvalues used in Eq. (20) are expressed as

$$T = \begin{bmatrix} 0 & 0 & \frac{\lambda_3 - \rho_\varepsilon U^1/b_2}{2\Delta} & \frac{\lambda_4 - \rho_\varepsilon U^1/b_2}{2\Delta} \\ \frac{\partial x}{\partial\eta} & \frac{\partial x}{\partial\zeta} & \frac{1}{2\Delta b_2}\frac{\partial\xi}{\partial x} & \frac{1}{2\Delta b_2}\frac{\partial\xi}{\partial x} \\ \frac{\partial y}{\partial\eta} & \frac{\partial y}{\partial\zeta} & \frac{1}{2\Delta b_2}\frac{\partial\xi}{\partial y} & \frac{1}{2\Delta b_2}\frac{\partial\xi}{\partial y} \\ \frac{\partial z}{\partial\eta} & \frac{\partial z}{\partial\zeta} & \frac{1}{2\Delta b_2}\frac{\partial\xi}{\partial z} & \frac{1}{2\Delta b_2}\frac{\partial\xi}{\partial z} \end{bmatrix}.$$

The inverse of the matrix T is of the form

$$T^{-1} = \frac{1}{|T|}\begin{bmatrix} 0 & \frac{\rho_\varepsilon}{2\Delta b_2^2}\left(\frac{\partial y}{\partial\zeta}\frac{\partial\xi}{\partial z} - \frac{\partial z}{\partial\zeta}\frac{\partial\xi}{\partial y}\right) & \frac{\rho_\varepsilon}{2\Delta b_2^2}\left(\frac{\partial z}{\partial\zeta}\frac{\partial\xi}{\partial x} - \frac{\partial x}{\partial\zeta}\frac{\partial\xi}{\partial z}\right) & \frac{\rho_\varepsilon}{2\Delta b_2^2}\left(\frac{\partial x}{\partial\zeta}\frac{\partial\xi}{\partial y} - \frac{\partial y}{\partial\zeta}\frac{\partial\xi}{\partial x}\right) \\ 0 & \frac{\rho_\varepsilon}{2\Delta b_2^2}\left(\frac{\partial z}{\partial\eta}\frac{\partial\xi}{\partial y} - \frac{\partial y}{\partial\eta}\frac{\partial\xi}{\partial z}\right) & \frac{\rho_\varepsilon}{2\Delta b_2^2}\left(\frac{\partial x}{\partial\eta}\frac{\partial\xi}{\partial z} - \frac{\partial z}{\partial\eta}\frac{\partial\xi}{\partial x}\right) & \frac{\rho_\varepsilon}{2\Delta b_2^2}\left(\frac{\partial y}{\partial\eta}\frac{\partial\xi}{\partial x} - \frac{\partial x}{\partial\eta}\frac{\partial\xi}{\partial y}\right) \\ \frac{|T|b_2}{\rho_\varepsilon} & -\frac{\lambda_4 - \rho_\varepsilon U^1/b_2}{2\Delta}\frac{\partial\xi}{\partial x} & -\frac{\lambda_4 - \rho_\varepsilon U^1/b_2}{2\Delta}\frac{\partial\xi}{\partial y} & -\frac{\lambda_4 - \rho_\varepsilon U^1/b_2}{2\Delta}\frac{\partial\xi}{\partial z} \\ -\frac{|T|b_2}{\rho_\varepsilon} & \frac{\lambda_3 - \rho_\varepsilon U^1/b_2}{2\Delta}\frac{\partial\xi}{\partial x} & \frac{\lambda_3 - \rho_\varepsilon U^1/b_2}{2\Delta}\frac{\partial\xi}{\partial y} & \frac{\lambda_3 - \rho_\varepsilon U^1/b_2}{2\Delta}\frac{\partial\xi}{\partial z} \end{bmatrix},$$

where $|T|=(\rho_\varepsilon/2\Delta b_2^2)(\partial\xi/\partial x_j)(\partial\xi/\partial x_j)\neq 0$.

The numerical flux $(\tilde{F}_1)_{j+1/2,k,l}$ in the ξ-direction for the three dimensional case is given by Eqs. (22) and (23), or Eq. (24) in terms of different spatial accuracies. The numerical fluxes in the other two directions can be calculated similarly in terms of the directional split method.[24]

It is noticed that after adding a preconditioned pseudotime derivative term (the first term) to the original system in Eq. (12) and moving the difference approximation of the physical time derivative term to the hand right side as a source term in Eq. (15), the time derivative preconditioned system of equations constructed here is now hyperbolic in pseudotime τ. The physical time coordinate is used to track the physical variation of the flow, whereas the pseudotime coordinate is used to march this system to a steady state at each physical time step. It is seen that Eq. (21) is expressed in an incremental form based on the flow variable difference between iterations $\Delta q=q^{n+1,m+1}-q^{n+1,m}$. Therefore, provided the solution converges in pseudotime (i.e., $\Delta q\rightarrow 0$ as $m\rightarrow\infty$), the left-hand side term goes to zero and the computed solution satisfies the original governing equations. In this study, the preconditioning methods are constructed to accelerate the convergence to a steady state and to produce a "better" artificial viscosity contribution (i.e., numerical dissipation terms) to stabilize the numerical scheme of the study and to improve accuracy through the upwind algorithms of Roe's approximate Riemann scheme and SCMM scheme. This is achieved by introducing the preconditioning matrix in Eq. (15) to make the speeds of all the waves (λ_1, λ_2, λ_3, *and* λ_4) in Eq. (27) closer to one another with appropriate definitions of V_r and $\Delta\tau$.

IV. NUMERICAL CALCULATIONS

To validate the mathematical model and numerical scheme of this study, it is necessary to confirm the application of the low Mach preconditioning dual-time stepping approach for general fluid flows in which compressibility effects range from weak to strong (e.g., $0\leq \mathrm{Ma}\leq 0.7$) before tackling two-phase compressible fluid sloshing problems. To develop confidence in the proposed model, we briefly examine subsonic and transonic compressible flows around a circular cylinder at free stream Mach numbers (Ma=0.001, 0.2, and 0.7) and assess the characteristics of these flows through comparison with published results.

A. Subsonic and transonic flows past a circular cylinder

The preconditioned Roe's flux-difference splitting scheme based on the primitive variables described in Sec. III A was used to determine the flow past a circular cylinder at free stream Mach numbers Ma=0.001, 0.2, and 0.7 and Reynolds number Re=200 based on a cylindrical diameter D and free stream velocity U_0. In this section, an O-shape grid size (99×81) was adopted with the computational boundary located at 14 diameters from the cylinder's center. Figure 1 illustrates the variation of drag coefficient against time and Mach number computed by the proposed mathematical model and these predictions are compared to an incompressible flow result evaluated using a different numerical flow solver.[21] All the curves have similar characteristics to the incompressible flow curve and the compressible result at Ma=0.001 shows near coincidence to it. This implies that the described preconditioning dual-time step method discussed previously is applicable to low Mach number flows without recourse to assuming the flow incompressible. Furthermore, the result for Ma=0.2 is in close agreement with the incompressible and Ma=0.001 flow calculations suggesting that if evidence exists that a compressible flow is in the region $\mathrm{Ma}\leq 0.2$, then compressibility effects can be ignored and equations, methods, and numerical schemes assuming incompressibility flow produce solutions of suitable accuracy. As can be seen, for Ma=0.7 the magnitude of the drag coefficient is greater than observed for $\mathrm{Ma}\leq 0.2$ although an oscillatory nature prevails. These findings are also confirmed by the calculations of pressure distributions (pressure coefficient $C_p=p/\rho U_0^2$) around the cylinder's surface at an instant, as shown in Fig. 2. These results show good agreement with similar predictions in literature,[27,28] which the interested reader may consult.

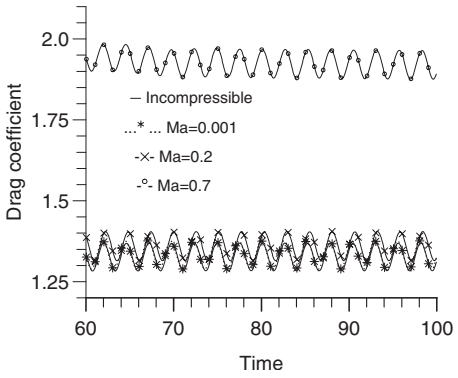

FIG. 1. Calculated time history of drag coefficient behavior associated with the flow past a circular cylinder at Reynolds number Re=200. The compressible flow solver result at Ma=0.001 compares favorably to the numerical result calculated using a different incompressible flow solver (Ref. 21).

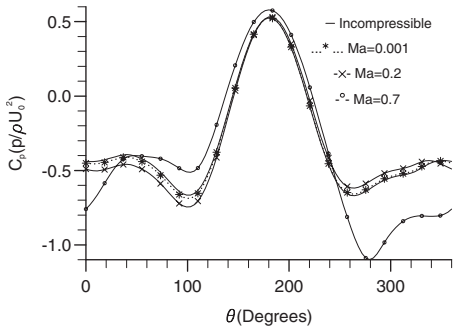

FIG. 2. Computed surface pressure coefficients for flow past a circular cylinder at Reynolds number Re=200. Again, the compressible flow solver result at Ma=0.001 compares favorably to the numerical result calculated using a different incompressible flow solver (Ref. 21).

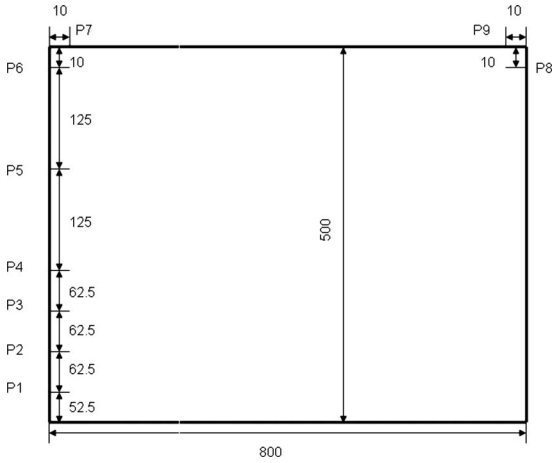

FIG. 3. Sloshing tank setup where the unit of length is millimeter, the letter P indicates the position of pressure sensor (P1, P2, …) at the center line of the tank of breadth of 400 mm.

B. Validation for liquid sloshing in a moving tank

To make sure that the proposed numerical method developed converges satisfactorily and to illustrate that it provides an acceptable accuracy to simulate impact pressures induced by sloshing, this section contains selected numerical examples of sloshing in an 80% filled tank subject to harmonic translational motions. The numerical results derived by the SCMM approach described in Sec. III B are compared to experimental data. It is noted that the mathematical model and numerical scheme of study are not restricted to a single motion excitation but allow combinations of motions (translations and rotations) in all degrees of freedom as well as irregular excitation inputs.

1. Experimental data

The experimental data[29] associated with sloshing in a rectangular tank of dimensions $0.8\times0.4\times0.5$ m^3, subject to harmonic sway motions of horizontal excitation amplitude $A=0.02$ m, are supplied by the Daewoo Shipbuilding and Marine Engineering Co., Ltd. Experimental results are available at all positions (P1, P2,…), as shown in the tank model in Fig. 3. The experimental measurements were recorded after the fluid was fully excited. Unfortunately, neither details of sensor size, characteristics, etc., nor the manner in which these records are obtained, i.e., filtering of signal, etc., are known and therefore the data are accepted at face value.

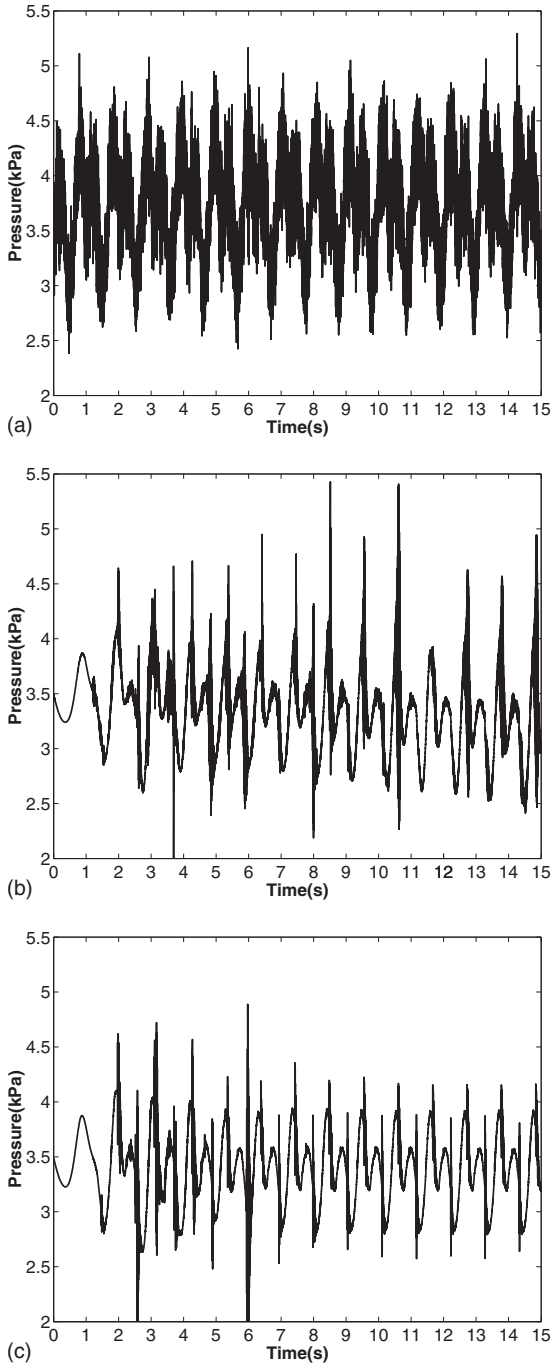

FIG. 4. Time histories of computed and measured pressure at position P1 ($\omega=1.0\omega_0$). (a) Measured; (b) compressible flow calculation (mesh: 161×101); (c) compressible flow calculation (mesh: 101×71).

2. Computational conditions

The media are assumed to be air and water with density of water $\rho_w=1025$ kg/m^3, and the reference density and pressure of air are $\rho_0=1.0$ kg/m^3 and $p_0=10^{+5}$ N/m^2 in Eq. (5), respectively. Unless otherwise stated, it is assumed that the fluid is inviscid and a slip boundary condition is applied to the rigid walls of the tank including the ceiling. The effect of surface tension is neglected in this investigation.

The initial conditions for all proceeding calculations are based on the tank moving from rest with the velocity components everywhere in the whole computational fluid domain set to zero. In all cases, the initial value of the level set function is set as the signed distance from the interface, positive in the air region, and negative in the fluid domain. The pressure distribution is defined by its hydrostatic value in the fluid below the interface and zero everywhere else, and the initial density values are evaluated from Eq. (10).

In this investigation, no special treatment is required for the free surface due to the two-fluid flow model adopted herein. A slip boundary condition is imposed by allowing the normal velocity to vanish at the wall. The pressure on the wall is obtained by projecting the momentum equation along the normal to the wall.

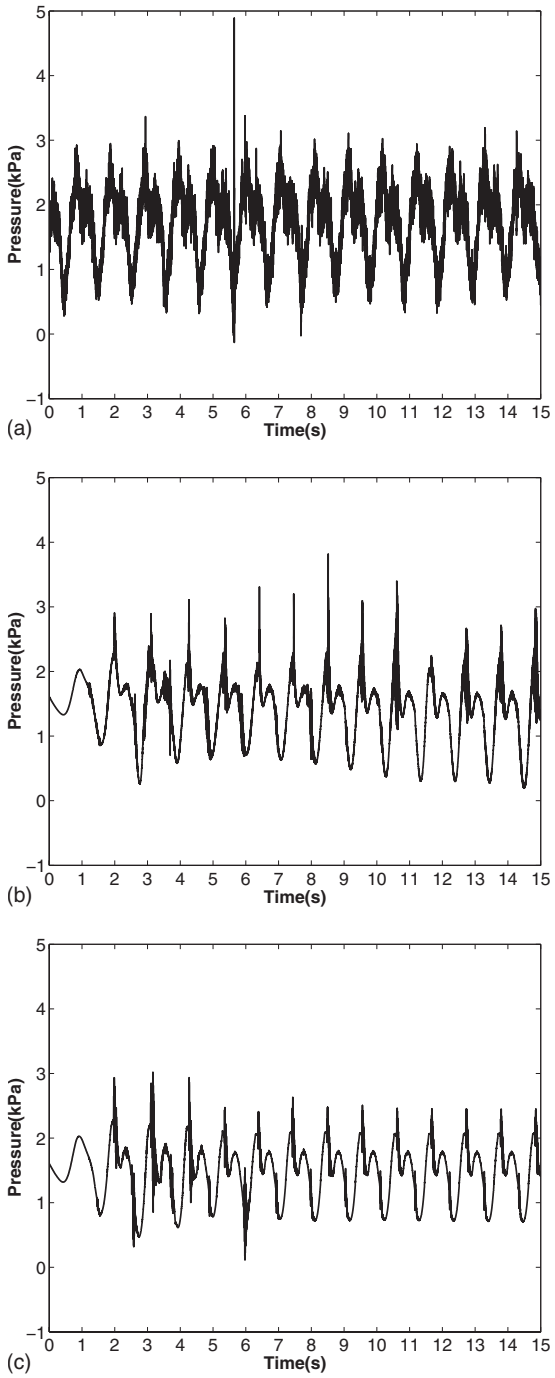

FIG. 5. Time histories of computed and measured pressure at position P4 ($\omega=1.0\omega_0$). (a) Measured; (b) compressible flow calculation (mesh: 161 $\times$101); (c) compressible flow calculation (mesh: 101$\times$71).

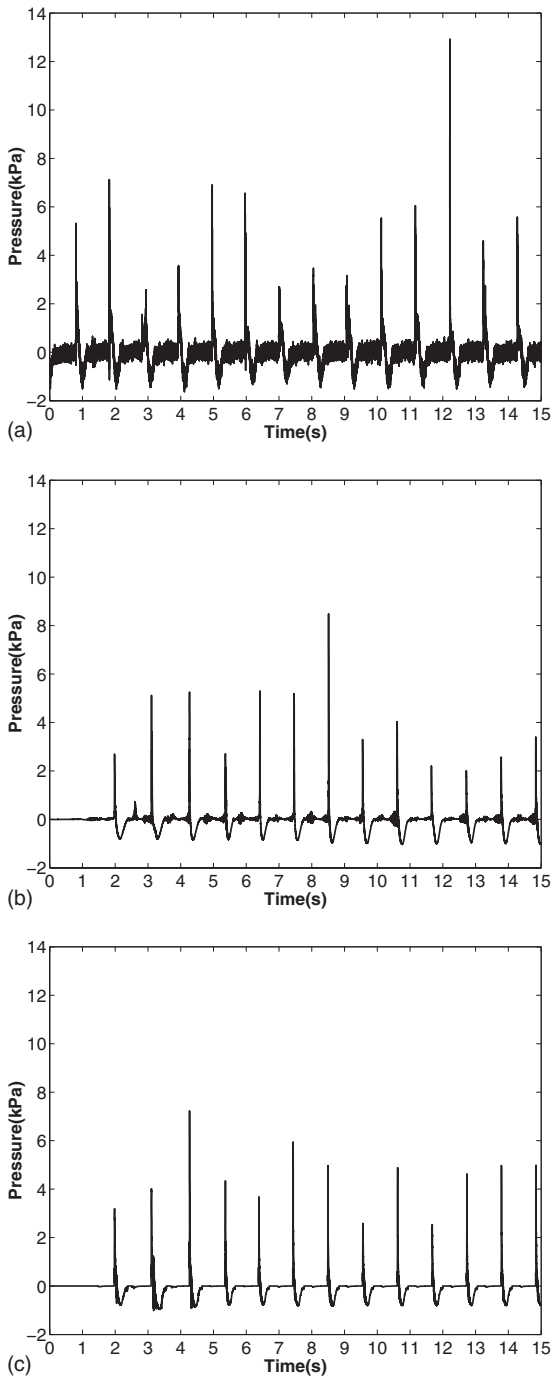

FIG. 6. Time histories of computed and measured pressure at position P7 ($\omega=1.0\omega_0$). (a) Measured; (b) compressible flow calculation (mesh: 161 $\times$101); (c) compressible flow calculation (mesh: 101$\times$71).

Numerical experiments revealed that the convergence of the presented numerical scheme of study is not very sensitive to the value of the pseudotime step increment $\Delta\tau$ when of the order of $(5\times10^{-5})-(1\times10^{-3})$ for two-fluid flow computations. For this reason, the value of $\Delta\tau=2\times10^{-4}$ was assumed for all test cases.

3. Resonance frequency excitation

The frequency of excitation considered in this section is set to $\omega=1.0\omega_0=0.945$ Hz (where ω_0 is the natural frequency of the rectangular tank) at resonance. Numerical calculations were performed using a 161$\times$101 uniform mesh and a 101$\times$71 nonuniform mesh. The time step increment used for both tests is set to $\Delta t=5\times10^{-4}$ s (approximately 2650 time steps in one oscillation). Figures 4–7 illustrate the comparisons between measured and computed pressure time histories at pressure gauge positions on the tank wall (P1 and P4) and ceiling (P7 and P9), as indicated in Fig. 3. For example, Figs. 4(a)–4(c) illustrate measured data and compressible simulations using the two different resolutions of mesh with similar findings shown in Figs. 5–7. The experimental measurements were recorded after the fluid was fully excited but the numerical simulations commenced from rest.

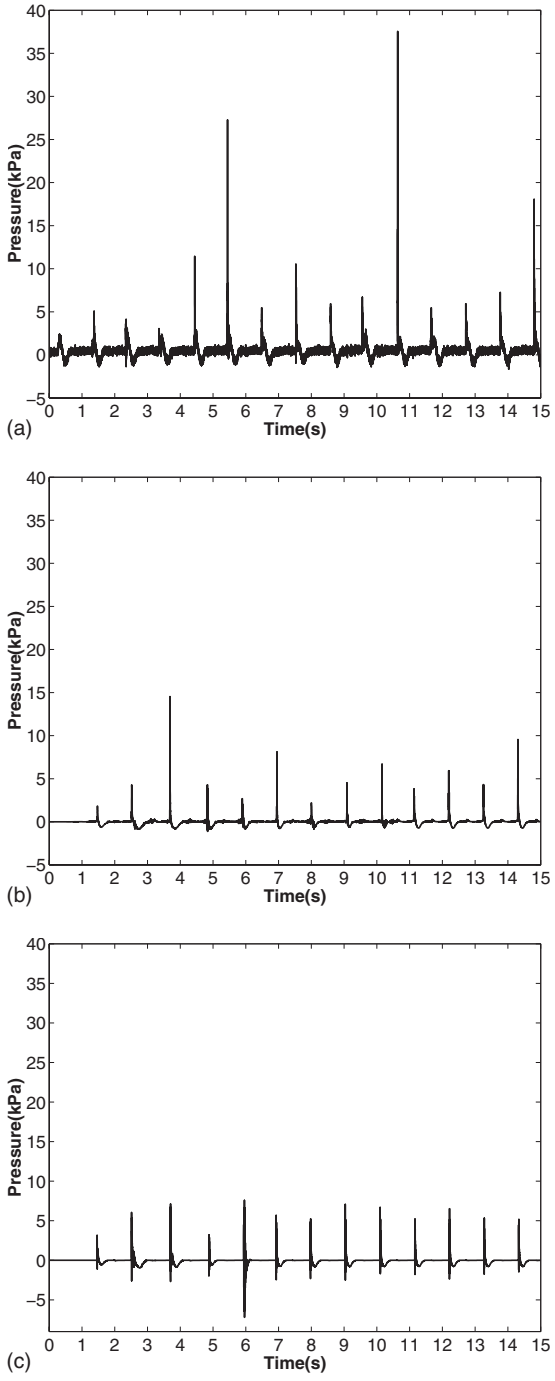

FIG. 7. Time histories of computed and measured pressure at position P9 ($\omega=1.0\omega_0$). (a) Measured; (b) compressible flow calculation (mesh: 161×101); (c) compressible flow calculation (mesh: 101×71).

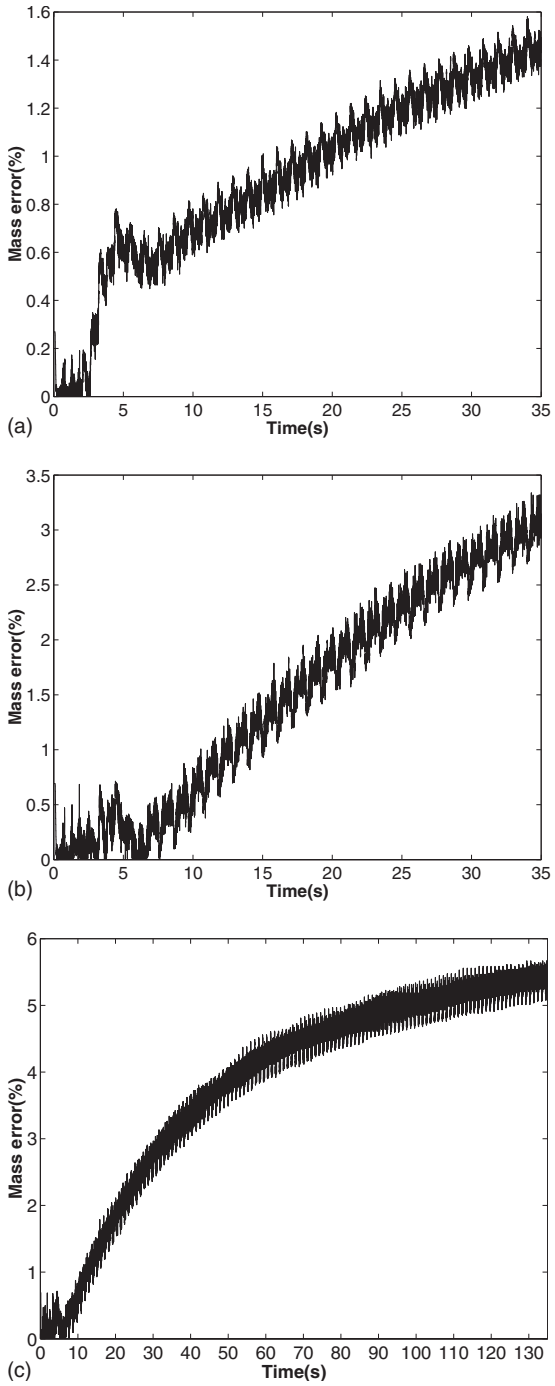

FIG. 8. Time history of liquid mass loss in the tank. (a) Mesh: 101×71; (b) mesh: 81×51 (up to 35 s); (c) mesh: 81×51 (up to 135 s)

In general, the computations produce the sloshing flow and dynamic characteristics of the measured data although pressure magnitudes show some discrepancies. At P1, Fig. 4, the three sets of data are of similar magnitudes and characteristics with the calculated results using the finer mesh closer to the measured data. At P4, Fig. 5, again a similar trend is observed. In Figs. 6 and 7 it is seen that the calculated peak values of the impact pressure acting on the tank's ceiling (P7) and its symmetric position (P9) are lower than the experimental values. This may be due to the introduction of the transition zone near the interface across which the density is smoothed.[21]

In order to test the performance of the present mathematical model and numerical scheme of study to conserve fluid mass during the violent sloshing, the simulation with the 101×71 mesh was run for approximately 35 s. Figure 8(a) shows the time history of liquid mass error defined by $\varepsilon_M=[|M(t)-M(0)|]/M(0)$, where $M(t)=\int_\Omega[1-H(\phi)]d\Omega$. In addition, a coarser size (81×51) mesh was used to investigate the trend of mass error with a longer running time of

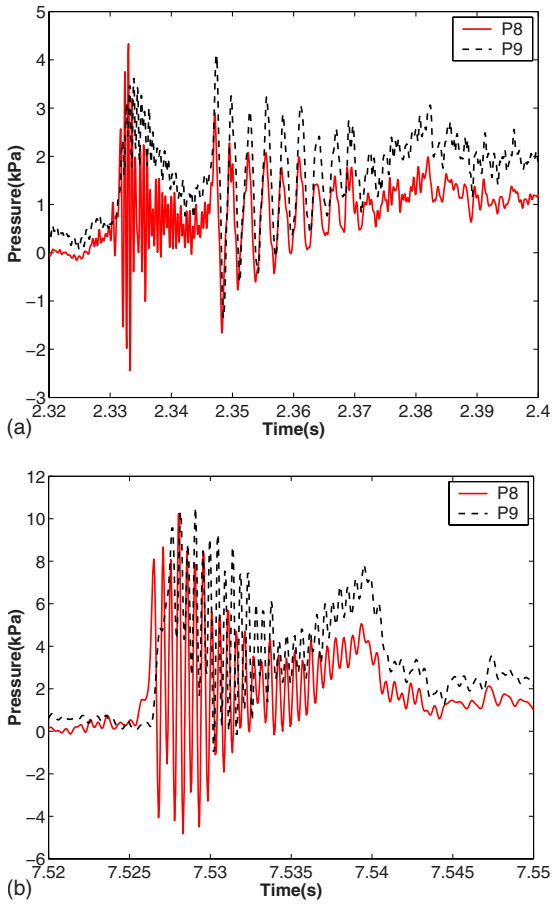

FIG. 9. (Color online) Time histories of measured pressures (Ref. 29) during impact inside the air pocket generated at two different times. (a) Impact pressure oscillation [the third measured impact event in Fig. 7(a)]; (b) impact pressure oscillation [the eighth measured impact event in Fig. 7(a)].

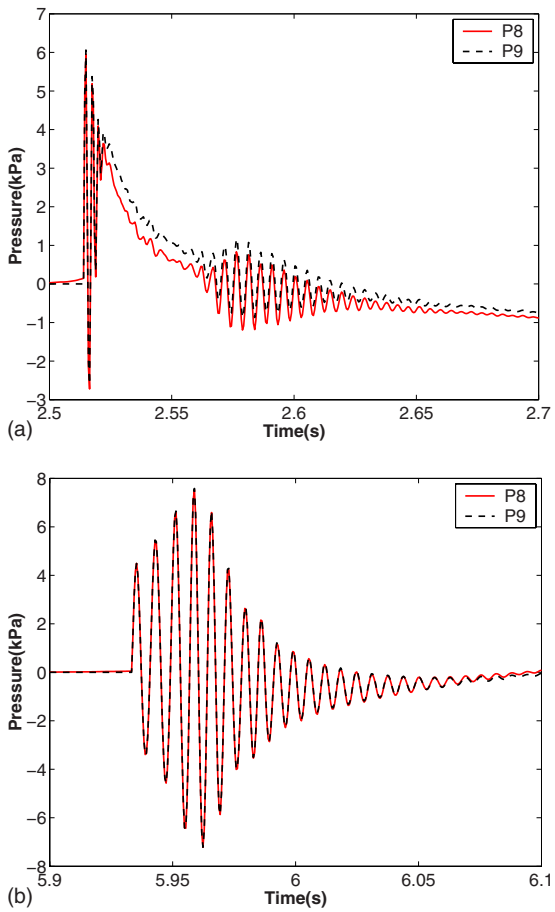

FIG. 10. (Color online) Time histories of calculated pressures during impact inside the air pocket generated at two different times (mesh: 101×71). (a) Impact pressure oscillation [the second impact event in Fig. 7(c)]; (b) impact pressure oscillation [the fifth impact event in Fig. 7(c)].

135 s, as shown in Fig. 8(b) (35 s) and Fig. 8(c) (135 s). It is noted that the mass error in Fig. 8(c) does not increase linearly against time, and the growth rate of mass error decreases with time. The finer mesh results are of the order of a half smaller, providing evidence that the finer the mesh the smaller the mass error, but the computational effort greatly increases.

For liquid sloshing in a rectangular tank with a high filling ratio, air cavities are often formed especially at the top corners of the tank. The trapped air acts like a mass-spring system (i.e., the air taking time to compress and then to expand) producing an underlying process that extends the duration of a pressure peak, decreases the magnitude of a pressure peak, and further causes a pressure oscillation following the peak. This oscillating pressure behavior is observed both experimentally[29] and numerically using the present model. For example, typical pressure signals inside air pockets recorded in the model test and in the numerical simulation at positions P8 and P9 at several instants are presented in Fig. 9 (measured) and Fig. 10 (calculated), respectively. It is noted that the amplitude and duration of impact pressure vary and have a random characteristic in different runs and even at different impact events in one run, depending on the free surface wave shape, liquid flow speed, and the size of the air cavity. A comparison of these figures shows similarities. For example, Figs. 9(a) and 10(a) demonstrate an implosion/explosion followed by an impact whereas Figs. 9(b) and 10(b) illustrate an impact only. The characteristics are similar although magnitude and duration of measurements and prediction are different.

As can be seen from these illustrative examples, the tracking or capturing of the interface, conservation of mass, etc., are of great importance to predict accurately fluid-structure interaction phenomena. For these reasons, other techniques[30,31] are under investigation by the authors to im-

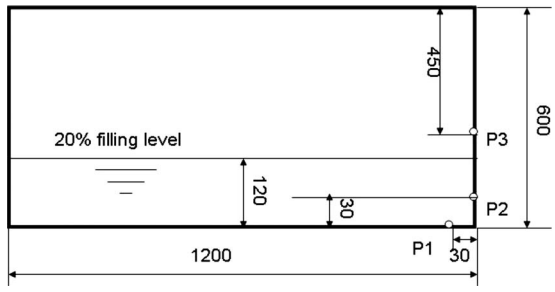

FIG. 11. Experimental setup of the rectangular tank (unit: millimeter).

TABLE I. Computational conditions for sloshing simulation inside a rectangular tank with 20% filling level.

Case	Mesh size	Time step (s)
A	95×51	$\Delta t=5\times10^{-4}$
B	121×61	$\Delta t=1\times10^{-3}$
C	145×75	$\Delta t=5\times10^{-4}$

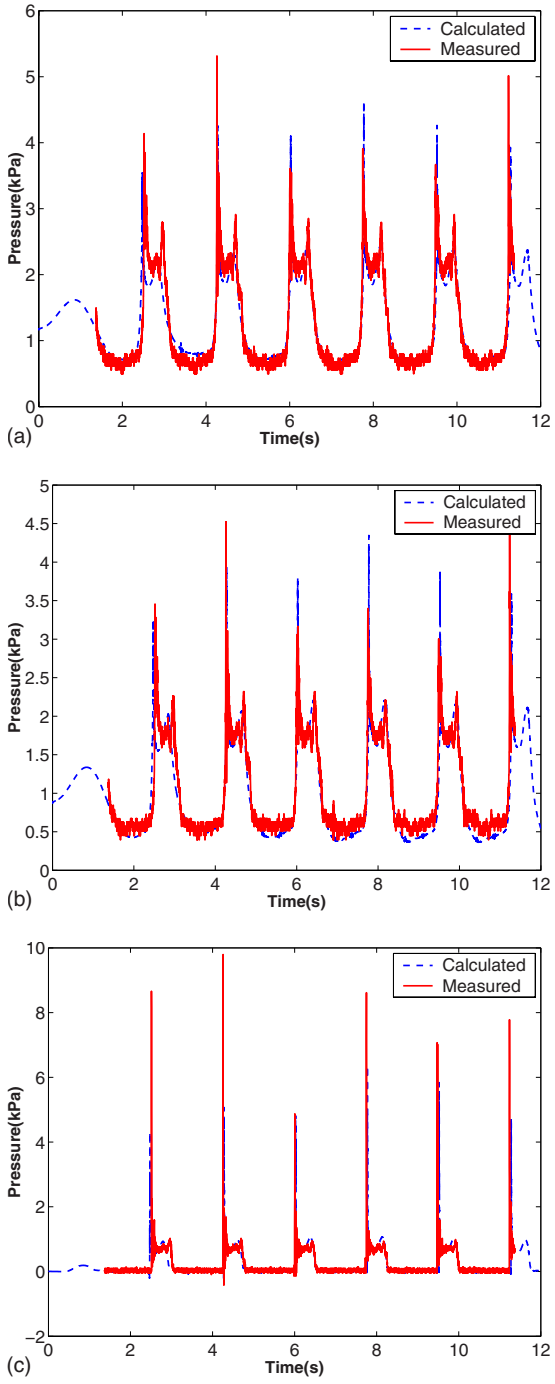

FIG. 12. (Color online) Comparison of time histories of pressure between measurement and calculation (case A). (a) P1; (b) P2; (c) P3.

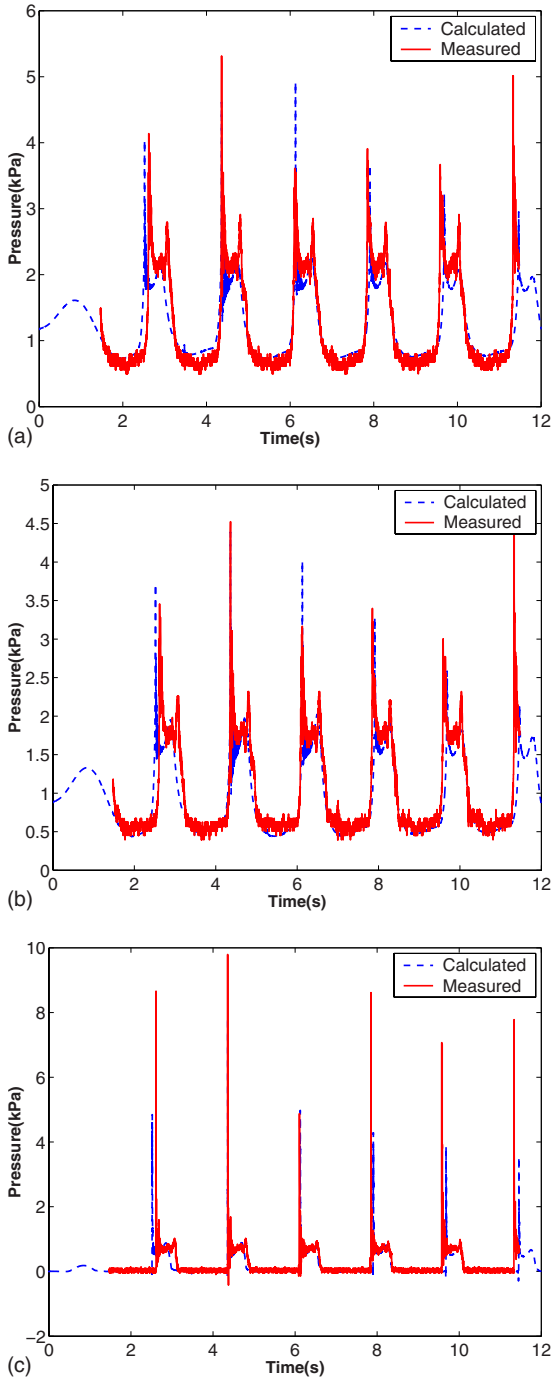

FIG. 13. (Color online) Comparison of time histories of pressure between measurement and calculation (case B). (a) P1; (b) P2; (c) P3.

prove the proposed numerical scheme of the study that has shown versatility in evaluating a wide of range of sloshing phenomena.

C. Sloshing induced impact against a vertical wall

The damage to tank walls by waves inside a tank has not been fully explained in fluid mechanical terms. High-speed photography reveals that the plume of water begins its upward motion from the water line with great acceleration. This rapidly rising motion of the free surface forming a jet was described by Peregrine[32] as flip through. In this section we

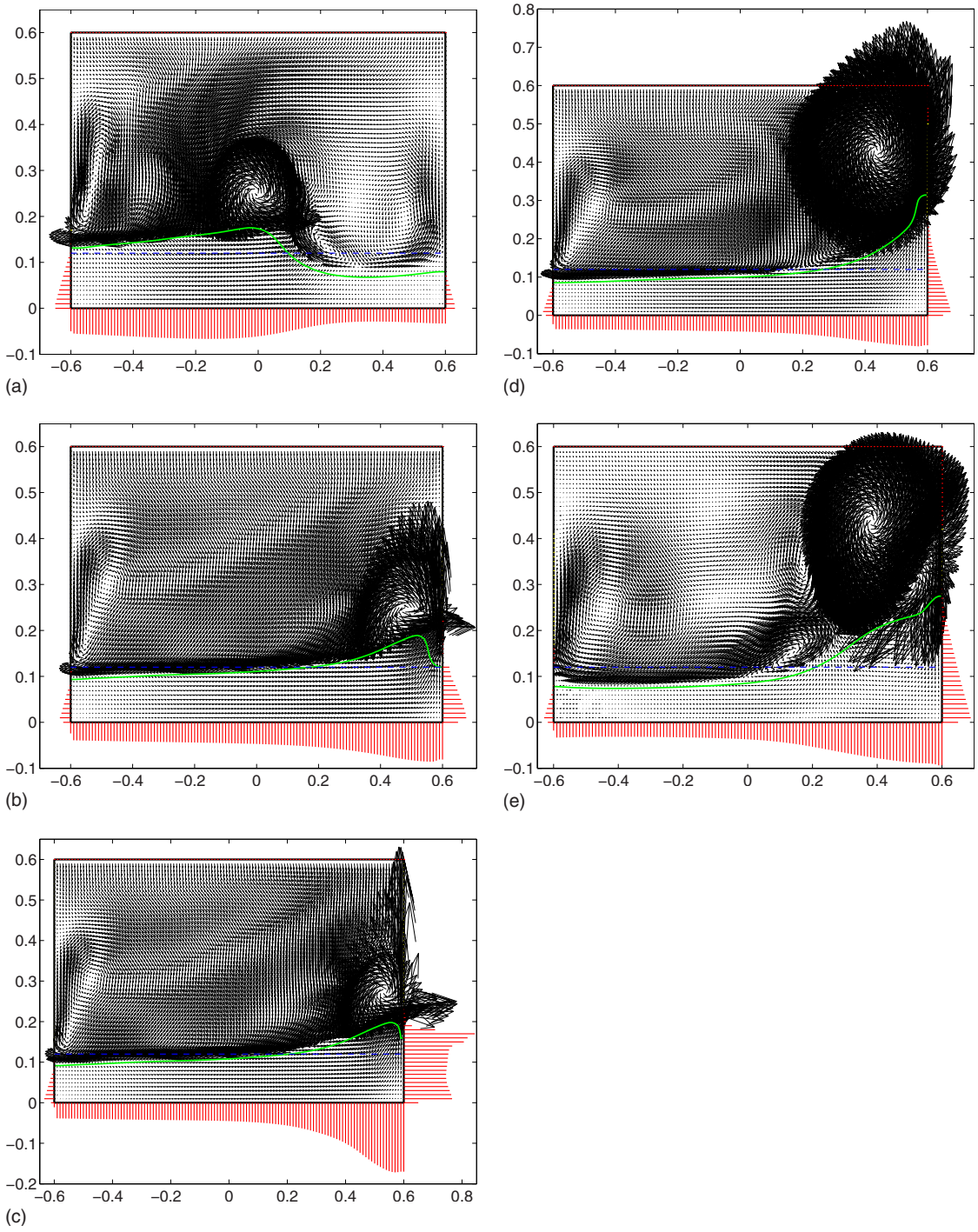

FIG. 14. (Color online) Wave motion snapshots during the first impact event at five different instants of time (case B). (a) Time=2.21 s; (b) time=2.50 s; (c) time=2.52 s; (d) time=2.60 s; (e) time=2.85 s.

carried out numerical simulation of water sloshing in a rectangular tank at a low filling level of 20%. The experimental data provided by Hinatsu *et al.*[33] are compared to calculated data derived by the discussed mathematical model herein. The experimental setup is sketched in Fig. 11. The tank is subject to an oscillating sway motion of the form $A\sin(\omega t)$. Here, the amplitude of forced motion is $A=60$ mm and the excited frequency is set to $\omega=1.74$ s at resonance. In order to demonstrate the efficiency of the developed method to simulate the complex impact phenomena, three test cases were performed to analyze the first impact event. The computational conditions for these three cases are listed in Table I.

The comparisons of calculated time histories of pressure with experiment at positions P1, P2, and P3 are shown in Fig. 12 (case A) and Fig. 13 (case B). These figures demonstrate very close agreement between experimental measurements and calculated results. In a more detailed analysis involving calculations at fixed times, Fig. 14 illustrates the first impact event for case B in which a wave is excited and

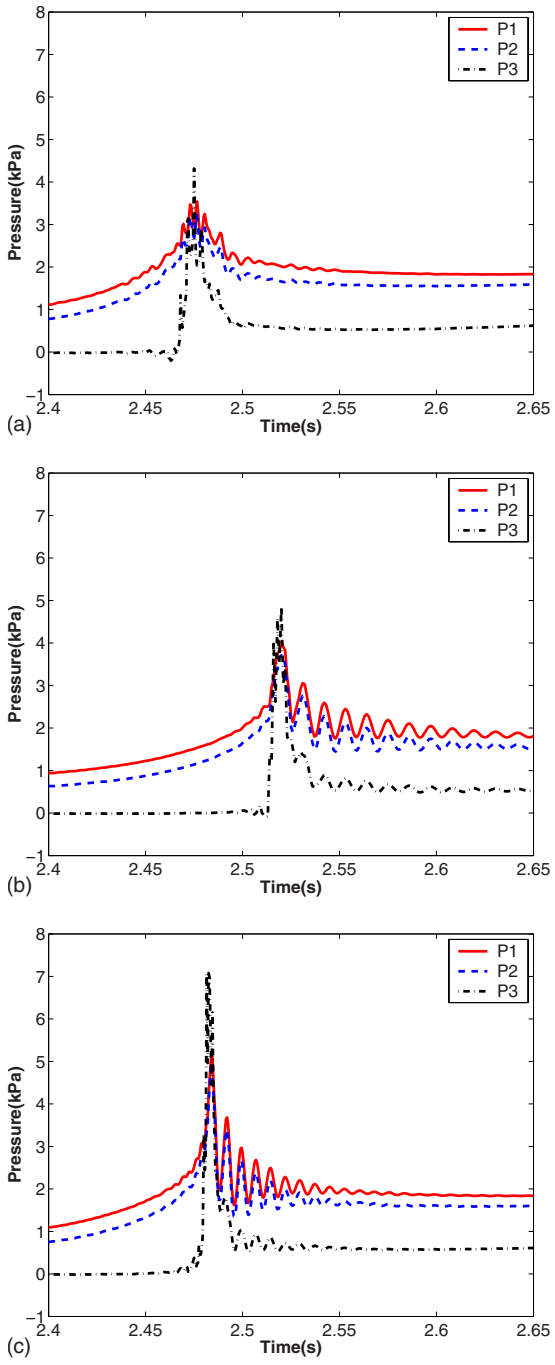

FIG. 15. (Color online) Time histories of the first impact pressure using different mesh size and time step increment. (a) Case A (mesh: 95×51; time step increment: $\Delta t=5\times10^{-4}$ s); (b) case B (mesh: 121×61; time step increment: $\Delta t=1\times10^{-3}$ s); (c) case C (mesh: 145×75; time step increment: $\Delta t=5\times10^{-4}$ s).

travels from left to right in the tank [i.e., Fig. 14(a)] breaking and trapping air [i.e., Fig. 14(b)] due to wave overturning in a violent motion before it impacts on the right wall. After the impact [i.e., Fig. 14(c)], water flows upward along the wall and then falls down due to gravity. Figure 14(c) shows the highest impact pressure occurring when the incident wave crest is almost parallel to the wall, and approaches with a velocity normal to the wall, whereas Figs. 14(d) and 14(e) provide evidence of the complex fluid motion after impact.

The overturning wave traps a pocket of air against the

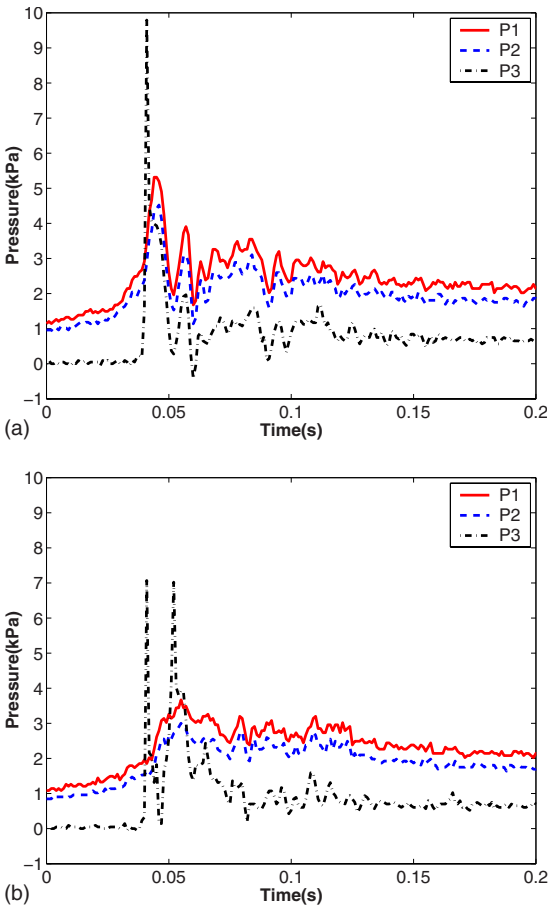

FIG. 16. (Color online) Time histories of measured pressure at two different impact events. (a) Corresponding to the second measured impact event in Fig. 12(c); (b) corresponding to the fifth measured impact event in Fig. 12(c).

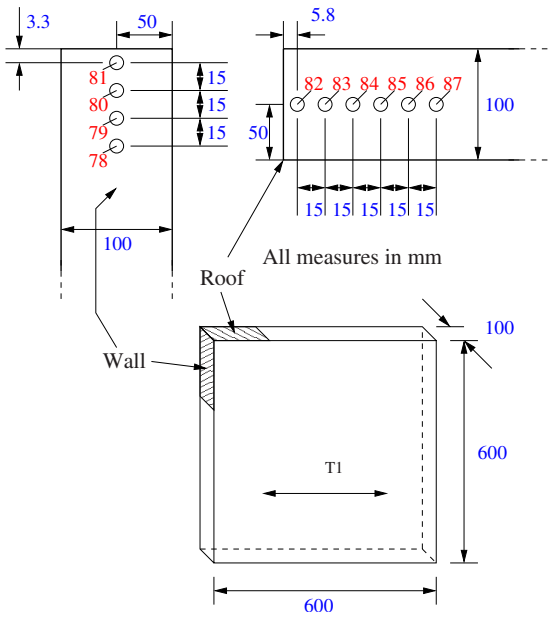

FIG. 17. (Color online) Experimental setup of tank used by Rognebakke and Faltinsen (Ref. 1) (unit: millimeter).

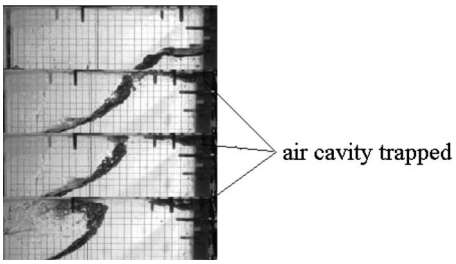

FIG. 18. Pictures of impact (Ref. 1) with air cavity at four instants (from top to bottom).

wall and this results in an increase in the duration of the pressure peak, with related reduction in peak pressure, and oscillations of pressure following the peak. Figure 15 presents short time histories of pressure oscillation at positions P1, P2, and P3 (see Fig. 11) during the first impact event for the three test cases. Figure 16 plots two time histories of measured pressure oscillation. Although mesh configurations and time steps are chosen differently, the characteristics of the signals show similarity with the finest mesh and shorter time step, i.e., Fig. 15(c), showing the highest peak pressures.

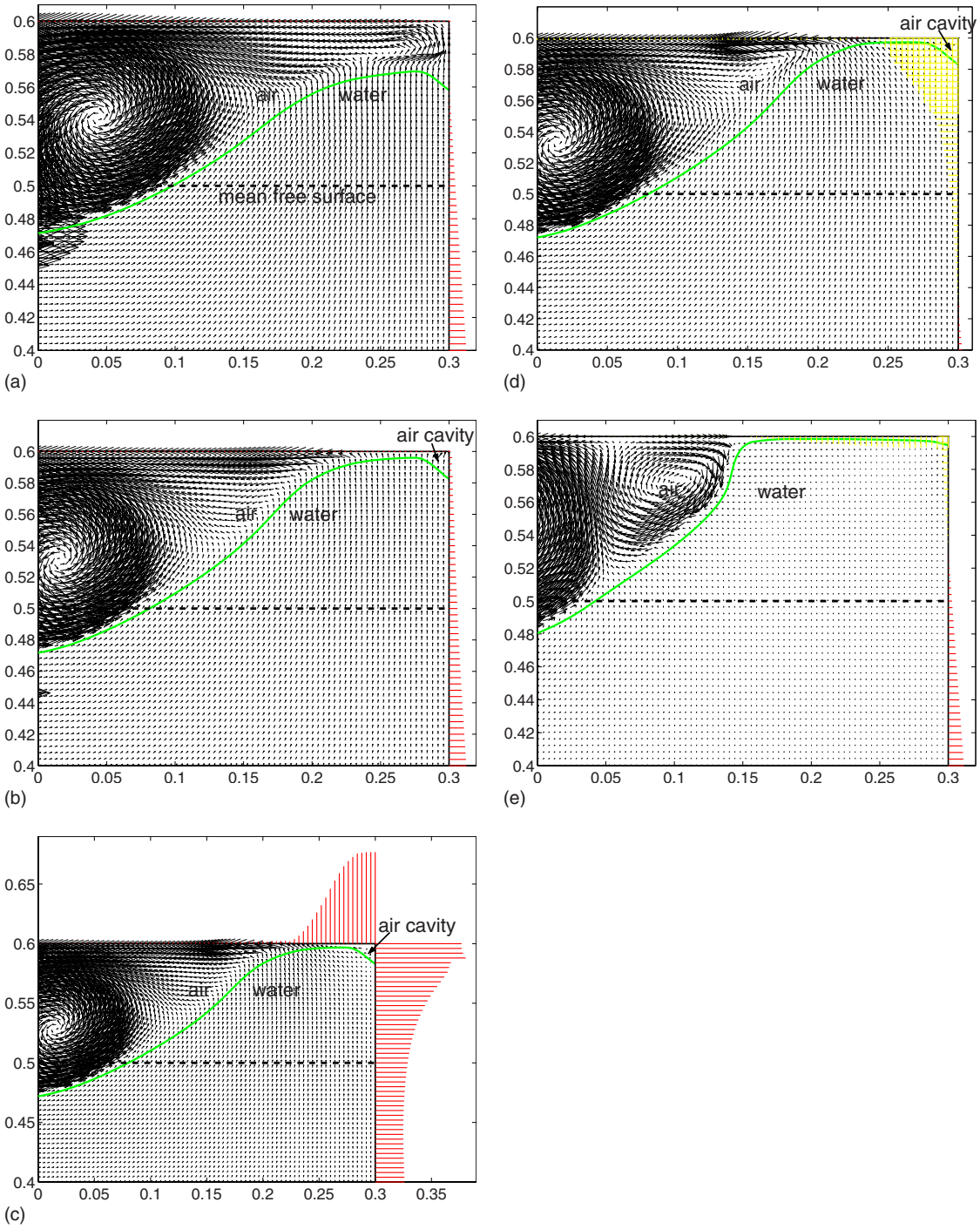

FIG. 19. (Color online) Pictures of computed free surface profile at five instants of time during an impact event (mesh: 151×151). (a) Time=0.0 s; (b) time=0.045 s; (c) time=0.0475 s; (d) time=0.05 s; (e) time=0.13 s.

D. Sloshing induced impact on tank roof with air cavity in a high filling ratio

In this section, the sloshing problem studied by Rognebakke and Faltinsen,[1] which involves an 83% full rectangular tank, is investigated. Figure 17 illustrates the dimensions of the tank and the distribution of pressure sensors inside the tank. Numerical simulations were conducted for the tank filled to a water depth of 500 mm and excited by a horizontal sway sinusoidal motion of amplitude $A=15$ mm and frequency $f=1.2$ Hz. In the numerical scheme of study, two uniform meshes with resolutions (121×121 and 151×151) are distributed inside the tank and both time steps are set to $\Delta t=5\times10^{-4}$ s.

Figure 18 illustrates the images[1] caught by a high-speed camera at four different time instants and these show an air cavity being trapped at the right top corner of the tank. It appears that this kind of impact with air cavity occurs frequently for a high filled ratio rectangular tank subject to regular translational motion. The calculated pressure exerted on the tank walls and roof, free surface profile, and flow velocity vector at several different instants are shown in Fig. 19 (fine mesh). They demonstrate the process of how a small air pocket at the right top corner of the tank is formed [see Figs. 19(a)–19(e)] and develops during the impact process. The numerical experiment indicates that the highest impact pressures occur when a small amount of air is trapped between the impacting wave and the tank top corner. It is also noted that for this case, where the air cavity is very small, most of the air leaks before it is completely enclosed. Figure 20 illustrates a comparison of the time histories of measured and calculated pressures using two size meshes during an impact. The simulations [Figs. 20(b) and 20(c)] correctly predict the amplitude of pressure oscillation but the oscillations exhibit more damped characteristic than observed in the experiment [Fig. 20(a)]. A further investigation is needed to understand the reason for this discrepancy as it appears dependent on mesh sensitivity [Figs. 20(b) and 20(c)] but overall, the proposed mathematical model and numerical scheme of study provide realistic descriptions of reality.

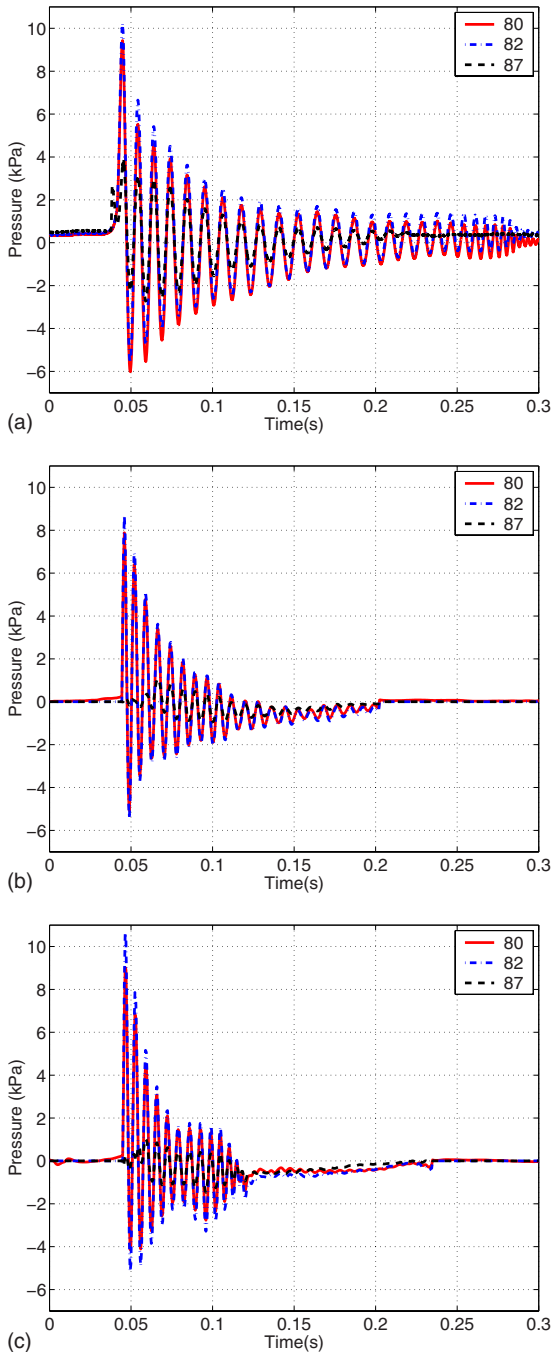

FIG. 20. (Color online) Time histories of pressure both measured and calculated during impact with air pocket formed. (a) Measured; (b) calculated (mesh: 121×121); (c) calculated (mesh: 151×151).

V. CONCLUSIONS

A mathematical model and numerical scheme of study are developed to examine single and two-fluid flows with the principal focus to simulate liquid sloshing in a partially filled tank. A successful scheme is devised based on the development of a low Mach number preconditioning dual-time stepping approach, a modified nonconservative implicit SCMM combined with a local level set method to capture free surface disturbances. This is demonstrated briefly by an investigation of the compressible flow around a circular cylinder at a range of Mach numbers (i.e., very weak flow to transition) and predictions compared to findings derived from adopting an incompressible flow solver[21] using a different numerical scheme. At Mach number Ma=0.001 (i.e., very weak subsonic flow) the compressible model produced results in very close agreement with those determined from the incompressible model demonstrating the applicability of the preconditioning dual-time stepping approach.

Predictions of sloshing in a partially filled tank assuming both fluids compressible were compared to experimental data.[28] The predicted characteristics of the time history data demonstrated reasonable agreement although absolute magnitudes indicated some discrepancies because of the appearance of more spikes in the calculated data than found experimentally. This requires further investigation both numerically and experimentally. Nevertheless, the predicted values were of the correct order of magnitude and of sufficient accuracy for preliminary design purposes.

The development of the theory described herein does not

necessitate an *a priori* assumption of incompressibility since it has been shown to adequately replicate this condition from the standpoint of compressibility. Furthermore, if and when strong compressibility effects occur in the sloshing problem (i.e., entrapped air arising in violent motions), it is able to take them into account and hence the developed dynamic mathematical model describes such physical phenomena and their influences with greater accuracy. This is demonstrated in comparisons of experimental observations[1,29,33] and numerical predictions.

ACKNOWLEDGMENTS

Y. G. Chen is grateful for the funding of this investigation from Lloyd's Register University Technology Centre, School of Engineering Sciences. The authors would like to express their gratitude to Dr. D. H. Kang and Dr. Y. B. Lee of the Daewoo Shipbuilding and Marine Engineering Co., LTD, South Korea in providing the experimental data for the first test case,[29] Dr. M. Hinatsu of the National Maritime Research Institute of Japan for the second test case,[33] and Dr. O. Rognebakke for providing the tank geometry and experimental details for the last test case.[1] The authors are also grateful to the referees for their valuable comments and constructive suggestions which have significantly enhanced the manuscript.

[1] O. Rognebakke, J. R. Hoff, J. Allers, K. Berget, B. O. Berge, and R. Zhao, "Experimental approaches for determining sloshing loads in LNG tanks," Transactions – Society of Naval Architects and Marine Engineers (SNAME), Houston, 2005.
[2] D. H. Peregrine and L. Thais, "The effect of entrained air in violent water wave impacts," J. Fluid Mech. **325**, 377 (1996).
[3] D. J. Wood, D. H. Peregrine, and T. Bruce, "Wave impact on a wall using pressure-impulse theory. I: Trapped air," J. Waterway, Port, Coastal, Ocean Eng. **126**, 182 (2000).
[4] C. Lugni, M. Brocchini, and O. M. Faltinsen, "Wave impact loads: The role of the flip-through," Phys. Fluids **18**, 122101 (2006).
[5] H. Bijl and P. Wesseling, "A unified method for computing incompressible and compressible flows in boundary-fitted coordinates," J. Comput. Phys. **141**, 153 (1998).
[6] H. Guillard and C. Viozat, "On the behaviour of upwind schemes in the low Mach number limit," Comput. Fluids **28**, 63 (1999).
[7] S. Venkateswaran, J. W. Lindau, R. F. Kunz, and C. L. Merkle, "Computation of multiphase mixture flows with compressibility effects," J. Comput. Phys. **180**, 54 (2002).
[8] B. Koren and B. van Leer, "Analysis of preconditioning and multigrid for Euler flows with low-subsonic regions," Adv. Comput. Math. **4**, 127 (1995).
[9] E. Turkel, "Preconditioning techniques in computational fluid dynamics," Annu. Rev. Fluid Mech. **31**, 385 (1999).
[10] W. R. Briley, L. K. Taylor, and D. L. Whitfield, "High-resolution viscous flow simulations at arbitrary Mach number," J. Comput. Phys. **184**, 79 (2003).
[11] S. A. Pandya, S. Venkateswaran, and T. H. Pulliam, "Implementation of preconditioned dual-time procedures in OVERFLOW," AIAA Paper No. 2003-0072, 2003.
[12] S. Karni, "Multicomponent flow calculations by a consistent primitive algorithm," J. Comput. Phys. **112**, 31 (1994).
[13] S. Karni, "Hybrid multifluid algorithms," SIAM J. Sci. Comput. (USA) **17**, 1019 (1996).
[14] B. Koren, M. R. Lewis, E. H. van Brummelen, and B. van Leer, "Riemann-problem and level set approaches for homentropic two-fluid flow computations," J. Comput. Phys. **181**, 654 (2002).
[15] J. P. Cocchi, R. Saurel, and J. C. Loraud, "Treatment of interface problems with Godunov-type schemes," J. Comput. Phys. **137**, 265 (1997).
[16] S. F. Davis, "An interface tracking method for hyperbolic systems of conservation laws," Appl. Numer. Math. **10**, 447 (1992).
[17] D. Igra and K. Takayama, "A high resolution upwind scheme for multicomponent flows," Int. J. Numer. Methods Fluids **38**, 985 (2002).
[18] R. Abgrall, "How to prevent pressure oscillations in multicomponent flow calculations: A quasi conservative approach," J. Comput. Phys. **125**, 150 (1996).
[19] R. P. Fedkiw, T. Aslam, B. Merriman, and S. Osher, "A non-oscillatory Eulerian approach to interfaces in multimaterial flows (the ghost fluid method)," J. Comput. Phys. **152**, 457 (1999).
[20] S. R. Chakravarthy, D. A. Anderson and M. D. Salas, "The split coefficient matrix method for hyperbolic systems of gas dynamic equations," AIAA Paper No. 80-0268, 1980.
[21] Y. G. Chen, K. Djidjeli, and W. G. Price, "Numerical simulation of liquid sloshing phenomena in partially filled containers," Comput. Fluids **38**, 830 (2009).
[22] M. Sussman, P. Smareka, and S. Osher, "A level set approach for computing solutions to incompressible two-phase flows," J. Comput. Phys. **114**, 146 (1994).
[23] M. Sussman, E. Fatemi, P. Smereka, and S. Osher, "An improved level set method for incompressible two-phase flows," Comput. Fluids **27**, 663 (1998).
[24] E. F. Toro, *Riemann Solvers and Numerical Methods for Fluid Dynamics: A Practical Introduction*, 2nd ed. (Springer-Verlag, Berlin, 1999).
[25] P. L. Roe, "Approximate Riemann solvers, parameter vectors and difference schemes," J. Comput. Phys. **43**, 357 (1981).
[26] C. K. Lombard, J. Bardina, E. Venkatapathy and J. Oliger, "Multi-dimensional formulation of CSSM: An upwind flux difference eigenvector split method for the compressible Navier–Stokes equations," AIAA Paper No. 83-1895, 1983.
[27] P. A. Berthelsen and O. M. Faltinsen, "A local directional ghost cell approach for incompressible viscous flow problems with irregular boundaries," J. Comput. Phys. **227**, 4354 (2008).
[28] R. Ghias, H. Mittal, and H. Dong, "A sharp interface immersed boundary method for compressible viscous flows," J. Comput. Phys. **225**, 528 (2007).
[29] D. H. Kang and Y. B. Lee, "Summary report of sloshing model test for rectangular model," Daewoo Shipbuilding and Marine Engineering Co., Ltd., Seoul, Report No. 001, 2005.
[30] T. Bonometti and J. Magnaudet, "Transition from spherical cap to toroidal bubbles," Phys. Fluids **18**, 052102 (2006).
[31] K. M. T. Kleefsman, G. Fekken, A. E. P. Veldman, B. Iwanowski, and B. Buchner, "A volume-of-fluid based simulation method for wave impact problems," J. Comput. Phys. **206**, 363 (2005).
[32] D. H. Peregrine, "Water-wall impact on walls," Annu. Rev. Fluid Mech. **35**, 23 (2003).
[33] M. Hinatsu, Y. Tsukada, R. Fukasawa, and Y. Tanaka, "Two-phase flows for joint research," *Proceedings of the SRI-TUHH Mini Workshop on Numerical Simulation of Two-Phase Flows*, edited by M. Hinatsu (National Maritime Research Institute Japan, Tokyo, 2001).